



Supplement of

Increased new particle yields with largely decreased probability of survival to CCN size at the summit of Mt. Tai under reduced SO₂ emissions

Yujiao Zhu et al.

Correspondence to: Likun Xue (xuelikun@sdu.edu.cn) and Xiaohong Yao (xhyao@ouc.edu.cn)

The copyright of individual parts of the supplement might differ from the CC BY 4.0 License.

List of Texts:

Text S1: Comparison of PM mass concentration derived from WPS with PM_{2.5} mass concentration measured by TEOM 1400a or Thermo 5030 SHARP.

Text S2: Calculations of new particle formation rate (FR), growth rate (GR), and condensation sink (CS).

Text S3: Underestimation of the ΔN_{CCN} and CS due to the lower upper size limit in 2007.

Text S4: Different VOCs analysis methods between 2006 and 2018.

List of Figures:

Figure S1: Annual emissions of SO₂ and annual average concentrations of SO₂, PM₁₀, and PM_{2.5} in China from 2007 to 2018 (data source: <http://www.stats.gov.cn/tjsj/ndsj/>, <http://www.mee.gov.cn/hjzl/zghjzkgb/lzghjzkgb/>).

Figure S2. The tree coverage areas around the sampling site in 2003 and 2016 based on MODIS satellite data (Black triangle represents the sampling site, data downloaded from <https://lpdaac.usgs.gov/products/mcd12c1v006/>).

Figure S3: Comparison of particle number concentration in 10-25 nm (a) and 10-300 nm (b) and the particle number size distribution (c) between WPS and SMPS during a summer campaign in 2020.

Figure S4. Unexpected errors of WPS around 213 nm on a non-NPF day (26 Mar 2018, a) and an NPF day (27 Mar 2018, b), and the raw (red) and corrected (purple) particle number size distribution on 27 Mar 2018 (c), the errors around 213 nm occurred for approximately 30% sampling days in 2017 and 2018.

Figure S5: The relationship between PM_{2.5} mass concentrations reported by TEOM 1400a (or Thermo 5030 SHARP) (x-axis) and PM mass concentrations derived from WPS (y-axis).

Figure S6: PNSD during 19:30-20:30 on April 23, 2007, i.e., $N_{CCN}(t_1)$.

Figure S7: Seasonal averages of ultraviolet (UV) radiation at the surface level from 2007 to 2018 (a, spring, b, summer, c, fall, d, winter). Open squares were seasonal averages, and solid circles were averaged during our sampling periods. Daily UV radiation data at 11:00 (UTC+8) were downloaded from <https://cds.climate.copernicus.eu/cdsapp#!/dataset/reanalysis-era5-single-levels?tab=form>).

Figure S8: Seasonal variations in particle number size distribution on NPF days in each campaign (shaded areas are quarter of the standard deviations).

Figure S9: Seasonal variations in particle number size distribution on non-NPF days in each campaign (shaded areas are quarter of the standard deviations).

Figure S10: Scatter plots between SO₂, H₂SO₄ and new particle formation rate (FR), net maximum increase in the nucleation-mode particle number concentration (NMINP).

Figure S11: Relationship between GR and NO₂+O₃ during NPF events.

Figure S12. Three types of NPF events, planetary boundary layer height (PBLH) and the 24-hour air mass back trajectories throughout the NPF events (a,b: Type A on March 21, 2018, c,d: Type b on April 7, 2018, e,f: Type c on September 29, 2014. Stars at the time axis represent the end time of trajectories, PBLH was downloaded from <https://goldsmr4.gesdisc.eosdis.nasa.gov>).

Text S1: Comparison of PM mass concentration derived from WPS with PM_{2.5} mass concentration measured by TEOM 1400a or Thermo 5030 SHARP.

The real-time PM_{2.5} mass concentrations were measured in 2007, 2014, 2017 and 2018. Assuming that the particle density as 1.5 g cm⁻³, the mobility diameter can be converted to the aerodynamic diameter with the equation: Aerodynamic diameter=Mobility diameter× $\sqrt{1.5}$. The particle mass concentration in each size bin could be calculated according to the particle number concentration reported by WPS. The sum of the mass concentrations of particles less than 2.3 μm in aerodynamic diameter (1.9 μm in mobility diameter) was compared with the PM_{2.5} mass concentration reported by TEOM 1400a (2007) or Thermo 5030 SHARP (2014-2018). The relationship of the hourly average data is shown in Fig. S5.

For the 2007 data, we calculated the mass concentration of PM_{0.18} from WPS and found that it has a weak correlation with PM_{2.5}. A slope of 0.05 indicated that the particles we observed accounted for only a minor fraction of the total mass of PM_{2.5}. For the two campaigns in 2014, the mass concentrations of WPS-derived PM_{2.3} and SHARP measured PM_{2.5} showed good correlations, with slopes of 0.69-0.76. For the 2017 and 2018 data, we removed the abnormal data in three bins around 213 nm. A good linear correlation was obtained between the two variables, but the slopes slightly increased to 0.86-0.9. Note that the calculation results depend on the adopted density of the particles. The actual particle density may deviate from the assumed value. In such cases, the sum volume (mass) may suffer from an error to some extent. The difference in the slopes may be partially related to the single value of particle density in different years, but other unknown factors cannot be excluded. Nevertheless, all of the deviations were less than 30%, and the linear correlations were generally good. However, the comparison alone cannot warrant the WPS operating properly.

Text S2: Calculations of new particle formation rate (FR), growth rate (GR), and condensation sink (CS)

The apparent formation rate of new particles (FR), considering the coagulation and growth losses, is calculated based on the following equation (Sihto et al., 2006; Kulmala et al., 2012; Zhu et al., 2019):

$$FR = \frac{dN_{10-25}}{dt} + CoagS_{10-25} \cdot N_{10-300} + \frac{GR_{10-25}}{15} \cdot N_{10-25} + S_{losses} \quad (1)$$

The coagulation loss for particles (CoagS₁₀₋₂₅·N₁₀₋₃₀₀) was the sum of particle-particle inter- and hetero-coagulation rates. The growth loss (GR₁₀₋₂₅/15·N₁₀₋₂₅) is due to condensation growth out of the nucleation mode sizes during the calculation period. S_{losses} includes additional losses and is assumed to be zero. In this equation, N₁₀₋₂₅ equals to N_{MINP}, and dN₁₀₋₂₅/dt equals to N_{MINP}/(t₁-t₀).The apparent

growth rate (GR) of new particles was calculated by:

$$GR = \frac{\Delta D_{pg}}{\Delta t} \quad (2)$$

where D_{pg} is the geometric median diameter of new particles fitted by the multiple log-normal distribution functions (Whitby, 1978; Zhu et al., 2014, 2019), and Δt is the duration for the growth of new particles.

The condensation sink (CS) is the loss rate of condensable vapor molecules onto the pre-existing particles, and calculated as Kulmala et al. (2001) and Dal Maso et al. (2005):

$$CS = 2\pi D \int D_p \beta_M(D_p) n(D_p) dD_p = 2\pi D \sum_i \beta_{Mi} D_{pi} N_{pi} \quad (3)$$

where D is the diffusion coefficient, β_M is the transitional regime correction factor, D_{pi} is the particle diameter of size class i , and N_{pi} is the particle number concentration in size class i .

Text S3: Underestimation of the ΔN_{CCN} and CS due to the lower upper size limit in 2007.

In this study, 10–300 nm particles were used to calculate ΔN_{CCN} and CS in all campaigns except for that in spring 2007. In the particular year, the data of >153 nm particles were missing. Alternatively, the data of 10–153 nm particles were used for the calculations. The lack of 153–300 nm particles may have led to the smaller ΔN_{CCN} and CS in 2007. Case analysis on the two issues is showed below:

Figure S6 shows the PNSD at 19:30–20:30 on April 23, 2007, when we calculated the CCN number concentrations, i.e., $N_{CCN}(t'_1)$. On that day, the maximum size of geometric median diameter of the grown new particles (D_{pgmax}) was the largest during the spring campaign in 2007. The lognormal fitted curve showed that approximately 15% of the area was missing to gain a complete accumulation mode, suggesting that $N_{CCN}(t'_1)$ was underestimated by ~15%. In other cases, the D_{pgmax} was smaller, and the missing areas in the PNSD curve caused even smaller underestimation.

We also calculated the CS in different size ranges, i.e., 10 nm–2.5 μm , 10 nm–300 nm and 10 nm–153 nm of particles in the campaign of 2018. The average CS values were $0.80 \pm 0.37 \times 10^{-2} \text{ s}^{-1}$, $0.75 \pm 0.34 \times 10^{-2} \text{ s}^{-1}$, and $0.40 \pm 0.15 \times 10^{-2} \text{ s}^{-1}$ for the three ranges of particles, respectively. The CS calculated by the use of particles in the range of 10 nm–300 nm accounted for 94% of those in the range of 10 nm–2.5 μm . Hence, the size range of 10–300 nm is sufficiently accuracy to estimate the condensational sink for comparing among different campaigns. However, the CS calculated by the use of particles in the range of 10 nm–153 nm accounted for only half of that in the range of 10 nm–2.5 μm . Thus, the CS calculated by the use of particles in the range of 10 nm–153 nm in 2018 was also used to compare with that in 2007.

Text S4: Different VOCs analysis methods between 2006 and 2018.

VOCs in the spring campaign of 2007 at Mt. Tai were not measured. Mao et al. (2009) measured the total VOCs at the same sampling site in June 2006, which were used for discussion. Mao et al. (2009) reported the measurements of 52 VOCs (C₄–C₁₂). The details on the method and the species of VOCs can be found therein. Theoretically, the temperature effect should increase BVOC emission more in June than those in spring. In the spring campaign of 2018, a total of 30 whole-air samples were collected for nine days. The collected VOCs were determined by gas chromatography (GC) separation, followed by flame ionization detection (FID), mass spectrometry detection (MSD), and electron capture detection (ECD) at a laboratory of the University of California at Irvine (UCI). 75 VOCs (C₂–C₁₀) non-methane hydrocarbons (NMHCs) were analyzed chemically. The analysis method of samples in 2018 has been reported by Chen et al. (2020). Note that a discrepancy on the measured VOCs between the two labs may exist and cause the uncertainty on the comparison to some extent.

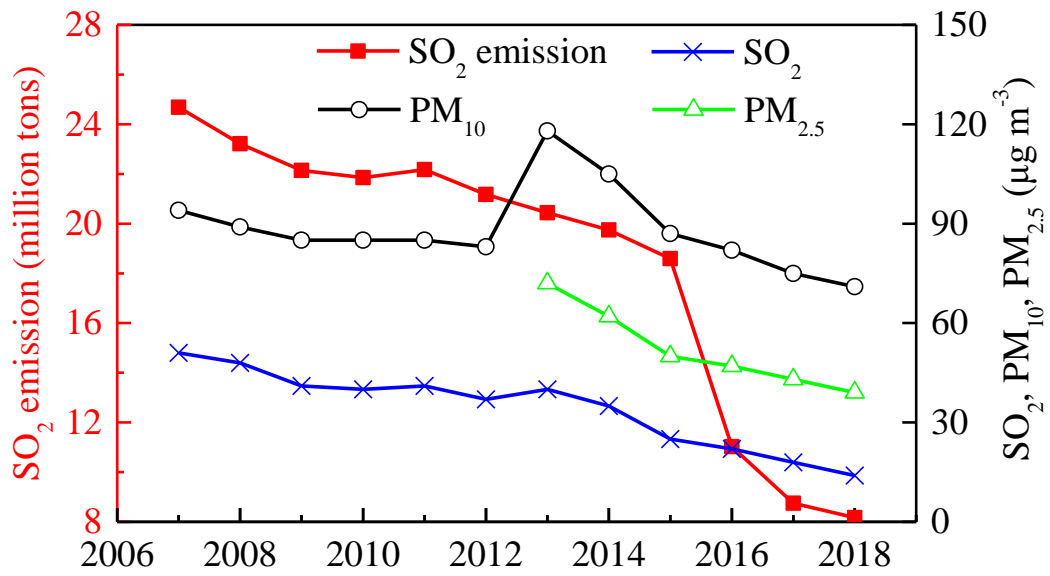


Figure S1. Annual emissions of SO₂ and annual average concentrations of SO₂, PM₁₀, and PM_{2.5} in China from 2007 to 2018 (data source: <http://www.stats.gov.cn/tjsj/ndsj/>, <http://www.mee.gov.cn/hjzl/zghjzkqb/lnzghjzkqb/>).

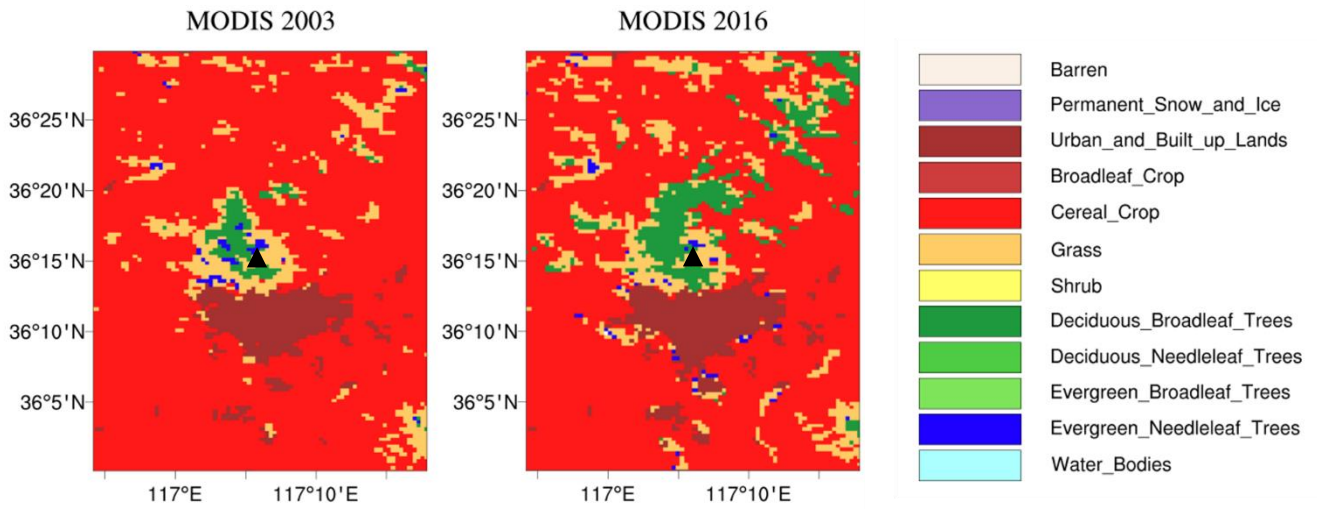


Figure S2. The tree coverage areas around the sampling site in 2003 and 2016 based on MODIS satellite data (Black triangle represents the sampling site, data downloaded from <https://lpdaac.usgs.gov/products/mcd12c1v006/>).

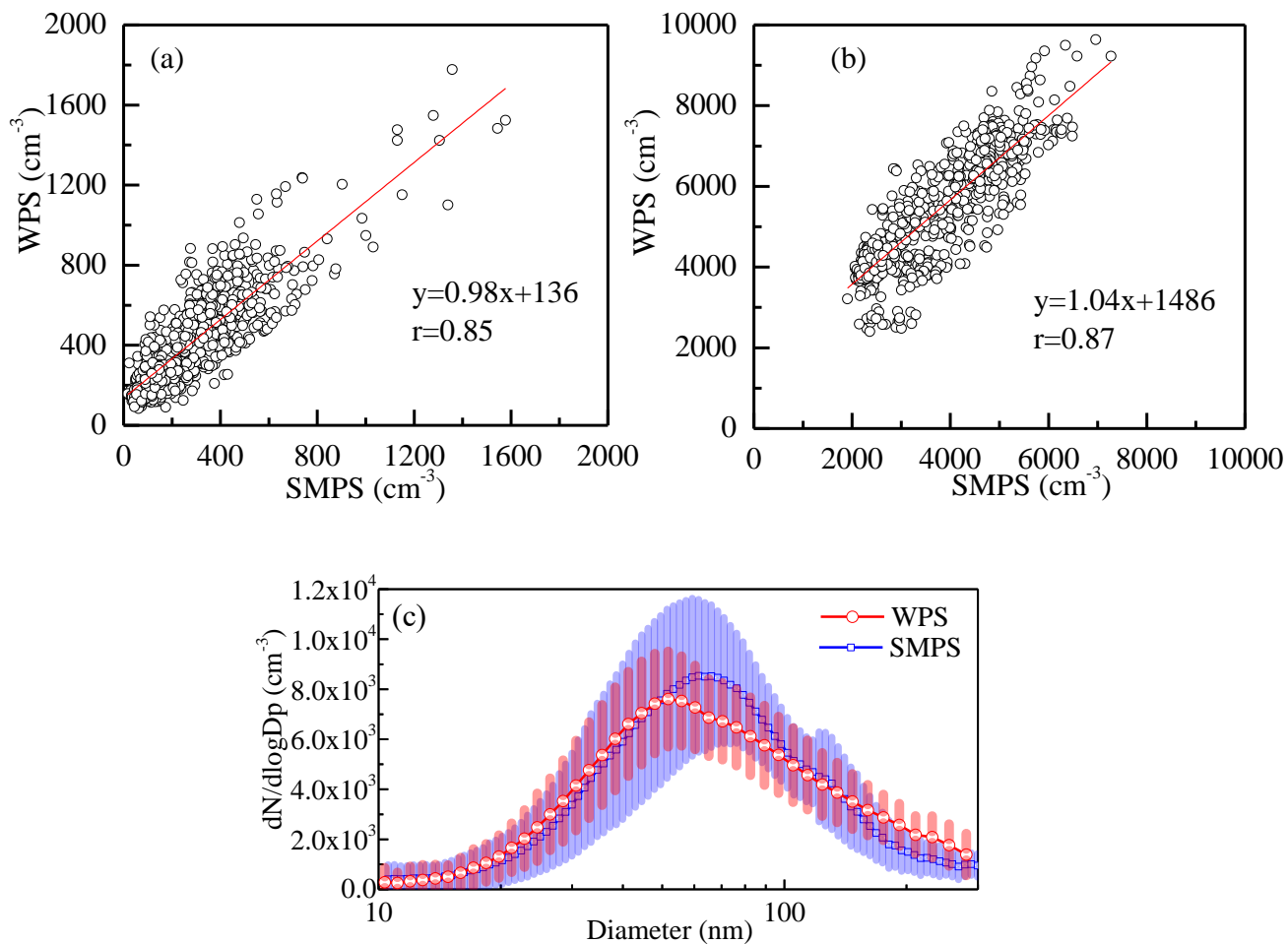


Figure S3: Comparison of particle number concentration in 10-25 nm (a) and 10-300 nm (b) and the particle number size distribution (c) between WPS and SMPS during a summer campaign in 2020.

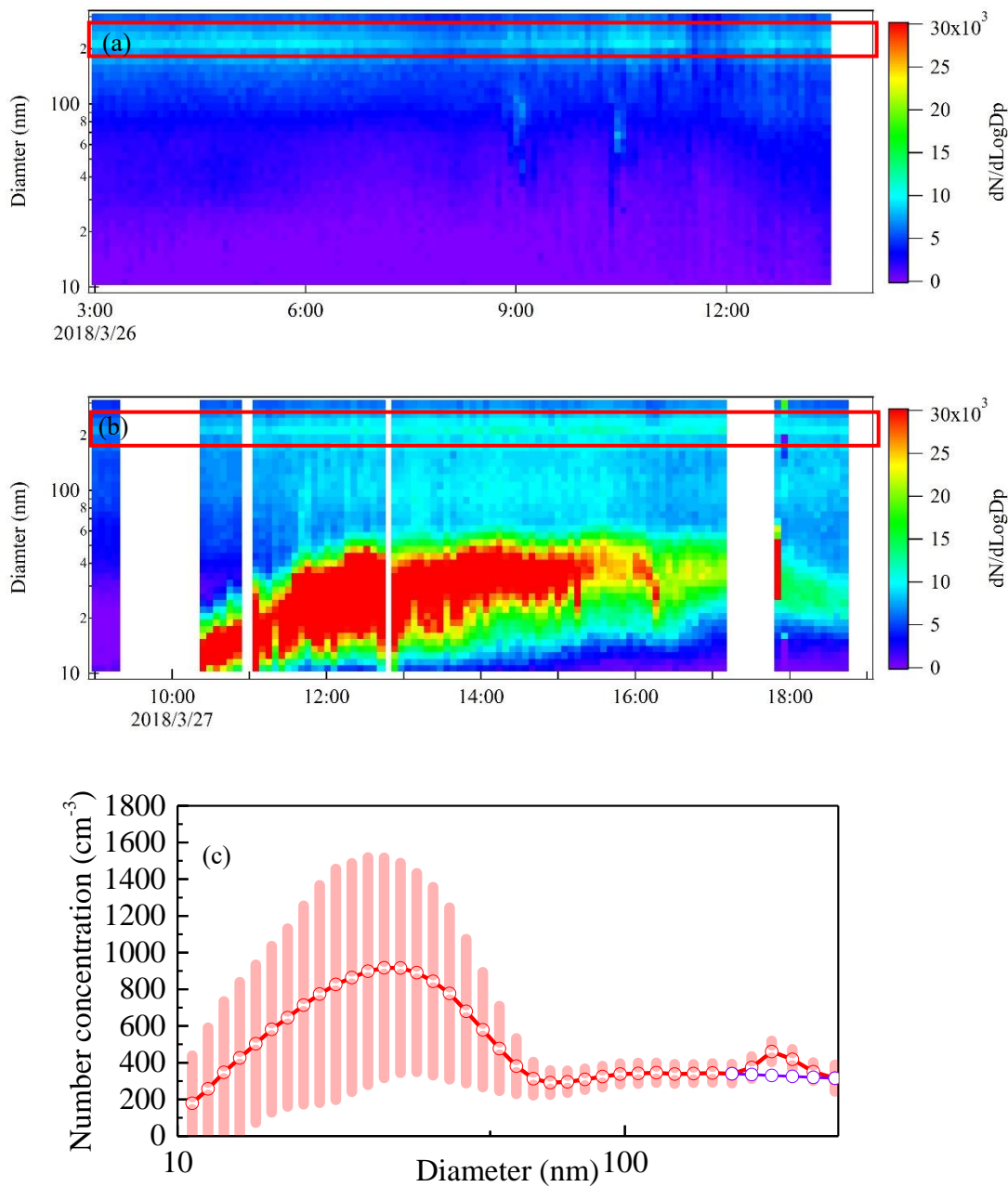


Figure S4. Unexpected errors of WPS around 213 nm on a non-NPF day (26 Mar 2018, a) and an NPF day (27 Mar 2018, b), and the raw (red) and corrected (purple) particle number size distribution on 27 Mar 2018 (c), the errors around 213 nm occurred for approximately 30% sampling days in 2017 and 2018.

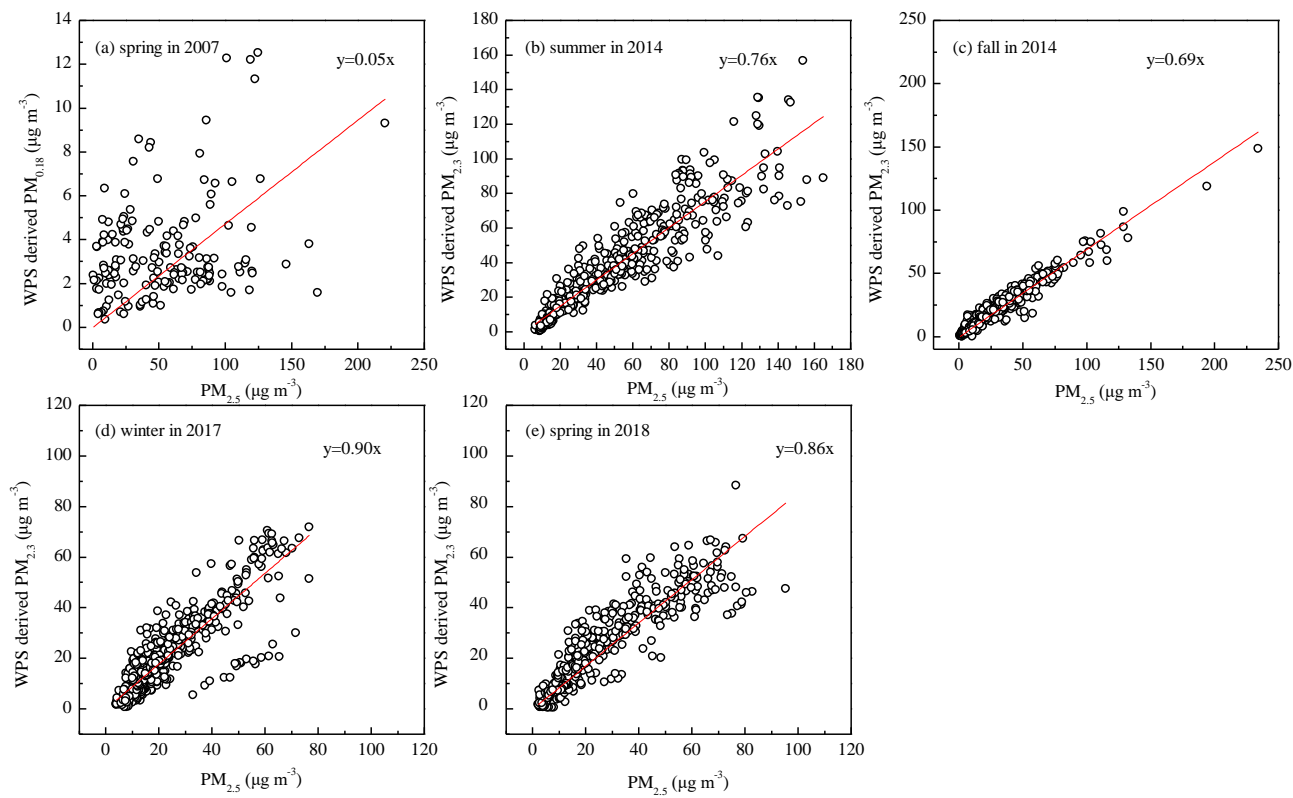


Figure S5: The relationship between PM_{2.5} mass concentrations reported by TEOM 1400a (or Thermo 5030 SHARP) (x-axis) and PM mass concentrations derived from WPS (y-axis).

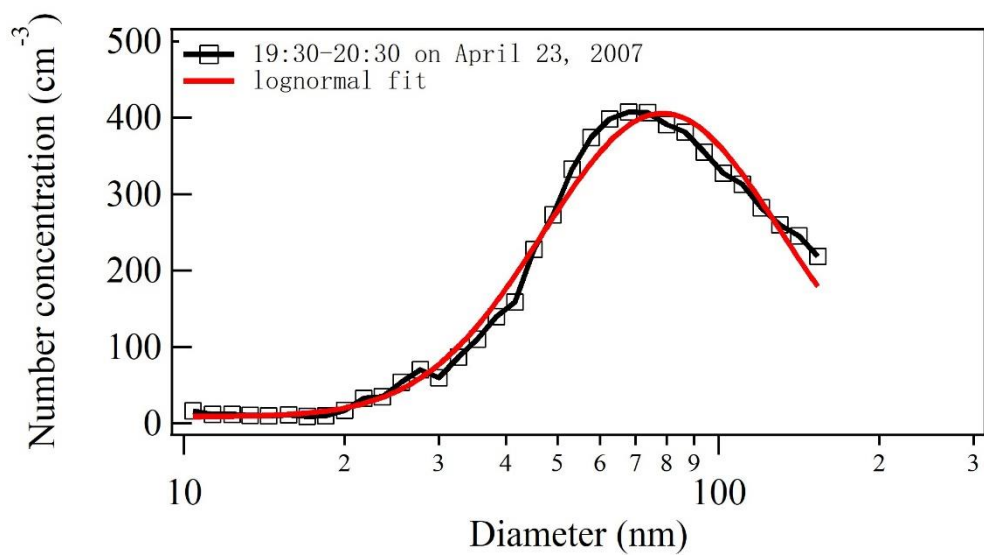


Figure S6 PNSD during 19:30-20:30 on April 23, 2007, i.e., $N_{CCN}(t'_1)$.

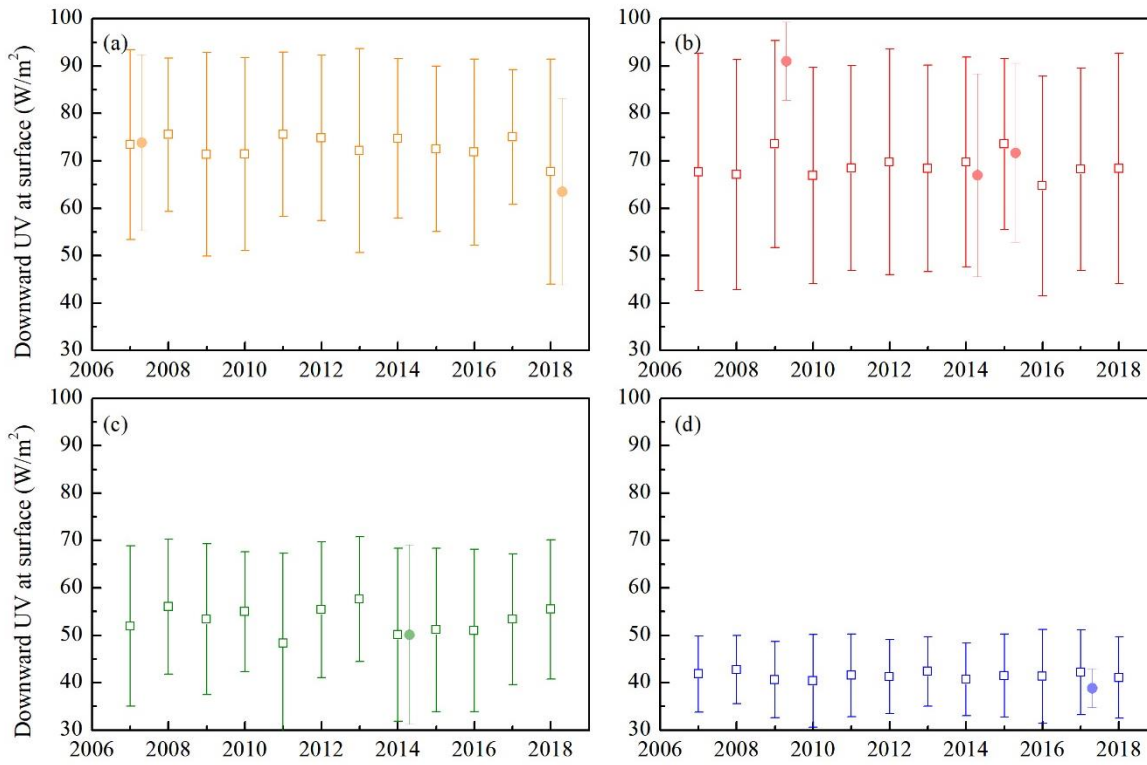


Figure S7: Seasonal averages of ultraviolet (UV) radiation at the surface level from 2007 to 2018 (a, spring, b, summer, c, fall, d, winter). Open squares were seasonal averages, and solid circles were averaged during our sampling periods. Daily UV radiation data at 11:00 (UTC+8) were downloaded from <https://cds.climate.copernicus.eu/cdsapp#!/dataset/reanalysis-era5-single-levels?tab=form>).

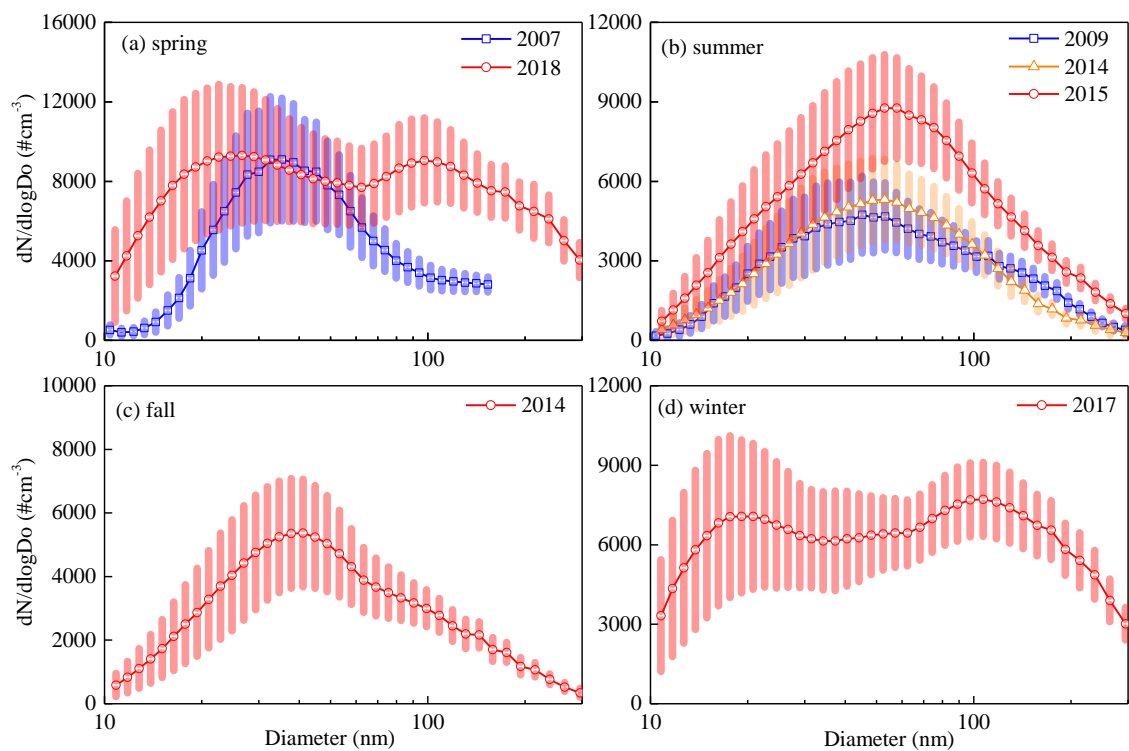


Figure S8: Seasonal variations in particle number size distribution on NPF days in each campaign (shaded areas are quarter of the standard deviations).

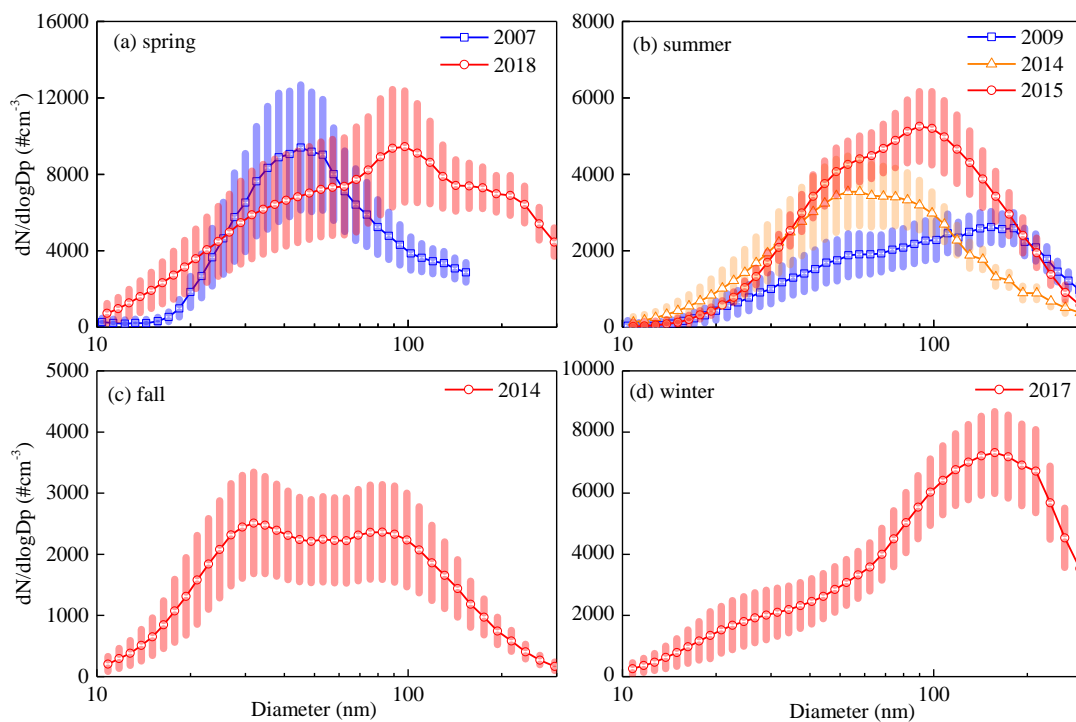


Figure S9: Seasonal variations in particle number size distribution on non-NPF days in each campaign (shaded areas are quarter of the standard deviations).

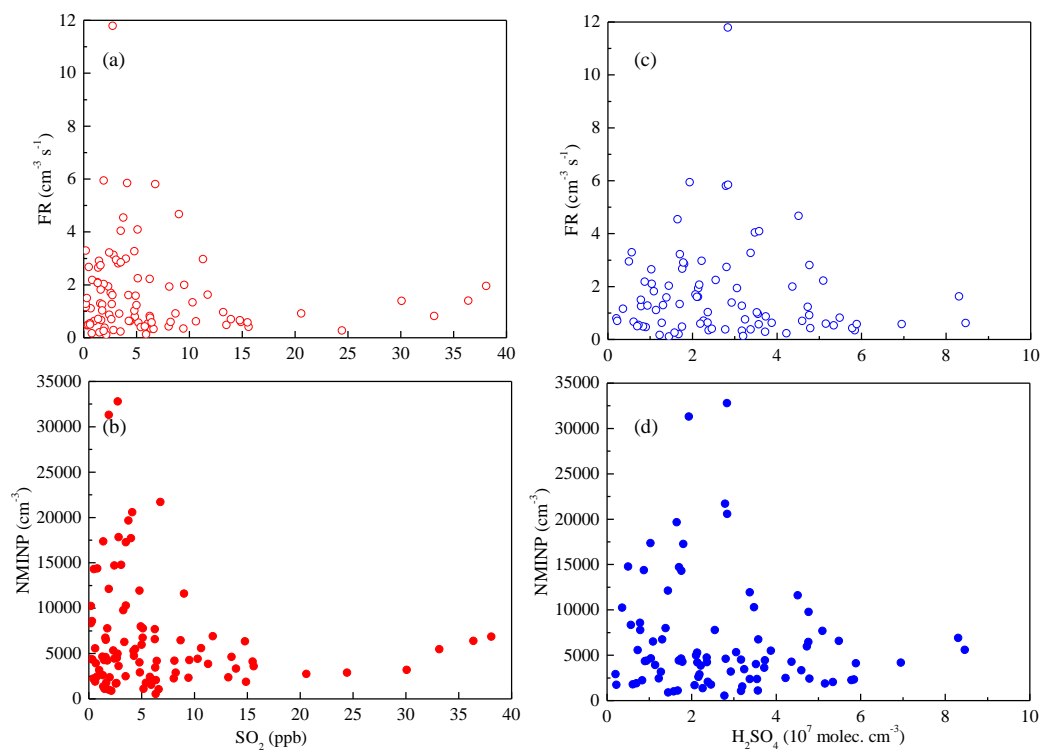


Figure S10. Scatter plots between SO₂, calculated H₂SO₄ and new particle formation rate (FR), net maximum increase in the nucleation-mode particle number concentration (NMIMP).

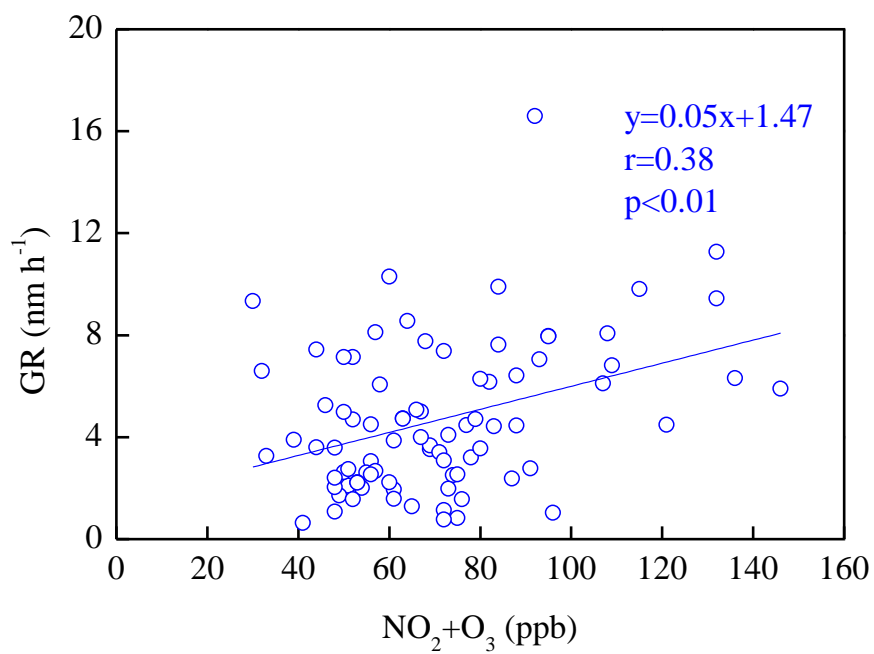


Figure S11. Relationship between GR and total oxidant ($O_x = NO_2 + O_3$) in the daytime NPF events.

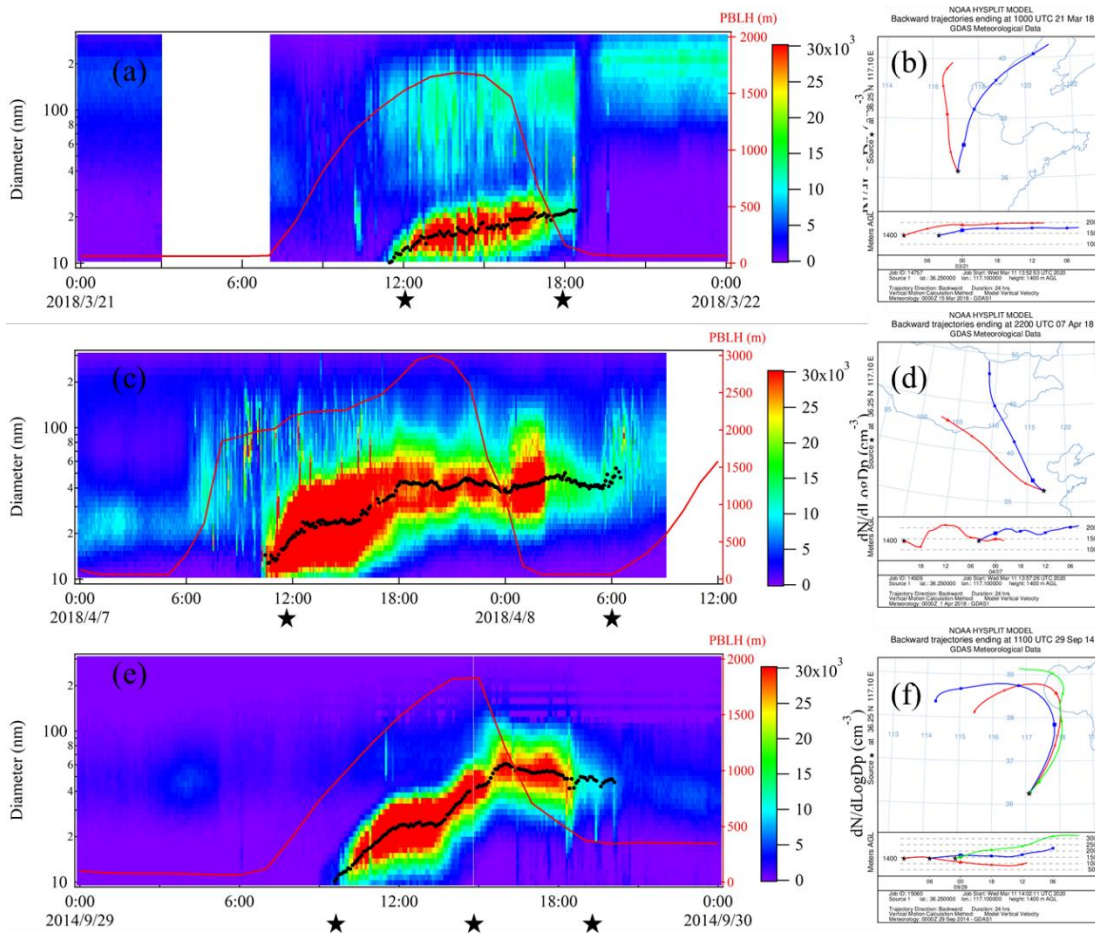


Figure S12. Three types of NPF events, planetary boundary layer height (PBLH) and the 24-hour air mass back trajectories throughout the NPF events (a,b: Type A on March 21, 2018, c,d: Type b on April 7, 2018, e,f: Type c on September 29, 2014. Stars at the time axis represent the end time of trajectories, PBLH was downloaded from <https://goldsmr4.gesdisc.eosdis.nasa.gov/data/MERRA2/M2T1NXFLX.5.12.4/>).

Reference:

- Dal Maso, M., Kulmala, M., Riipinen, I., Wagner, R., Hussein, T., Aalto, P. P., and Lehtinen, K. E. J.: Formation and growth of fresh atmospheric aerosols: Eight years of aerosol size distribution data from SMEAR II, Hyytiälä, Finland, *Boreal Environ. Res.*, 10, 323–336, 2005.
- Kulmala, M., Dal Maso, M., Mäkelä, J. M., Pirjola, L., Väkevä, M., Aalto, P., Miikkulainen, P., Hämeri, K., O'Dowd, C. D. On the formation, growth and composition of nucleation mode particles. *Tellus B*, 53(4), 479-490, 2001.
- Kulmala, M., Petäjä, T., Nieminen, T., Sipilä, M., Manninen, H. E., Lehtipalo, K., Dal Maso, M., Aalto, P. P., Junninen, H., Paasonen, P., Riipinen, I., Lehtinen, K. E. J., Laaksonen, A., and Kerminen, V.-M.: Measurement of the nucleation of atmospheric aerosol particles, *Nat. Protoc.*, 7, 1651–1667, <https://doi.org/10.1038/nprot.2012.091>, 2012.
- Mao, T., Wang, Y., Xu, H., Jiang, J., Wu, F., and Xu, X.: A study of the atmospheric VOCs of Mount Tai in June 2006, *Atmos. Environ.*, 43, 2503-2508, <https://doi.org/10.1016/j.atmosenv.2009.02.013>, 2009.
- Sihto, S.-L., Kulmala, M., Kerminen, V.-M., Dal Maso, M., Petäjä, T., Riipinen, I., Korhonen, H., Arnold, F., Janson, R., Boy, M., Laaksonen, A., and Lehtinen, K. E. J.: Atmospheric sulphuric acid and aerosol formation: implications from atmospheric measurements for nucleation and early growth mechanisms, *Atmos. Chem. Phys.*, 6, 4079–4091, <https://doi.org/10.5194/acp-6-4079-2006>, 2006.
- Whitby, K. T.: The physical characteristics of sulfur aerosols, *Atmos. Environ.*, 12, 135-159, 1978.
- Zhu, Y., Sabaliauskas, K., Liu, X., Meng, H., Gao, H., Jeong, C. H., Evans, G. J., and Yao, X.: Comparative analysis of new particle formation events in less and severely polluted urban atmosphere, *Atmos. Environ.*, 98, 655–664, <https://doi.org/10.1016/j.atmosenv.2014.09.043>, 2014.
- Zhu, Y., Li, K., Shen, Y., Gao, Y., Liu, X., Yu, Y., Gao, H., and Yao, X.: New particle formation in the marine atmosphere during seven cruise campaigns, *Atmos. Chem. Phys.*, 19, 89–113, <https://doi.org/10.5194/acp-19-89-2019>, 2019.